Received September 21, 2021, accepted October 7, 2021, date of publication October 13, 2021, date of current version October 25, 2021.

Digital Object Identifier 10.1109/ACCESS.2021.3119565

Target Adaptive Differential Iterative Reconstruction (TADI): A Robust Algorithm for Real-Time Electrical Impedance Tomography

WEIRUI ZHANG[1], TAO ZHANG[1,2], XUECHAO LIU[1], BIN YANG[1], MENG DAI[1], XUETAO SHI[1], XIUZHEN DONG[1], (Member, IEEE), FENG FU[1], AND CANHUA XU[1]

[1]Department of Biomedical Engineering, Fourth Military Medical University, Xi'an 710032, China
[2]Drug and Instrument Supervision and Inspection Station, Xining Joint Logistics Support Center, Lanzhou 730050, China

Corresponding authors: Canhua Xu (canhuaxu@fmmu.edu.cn) and Feng Fu (fengfu@fmmu.edu.cn)

This work was supported in part by the National Natural Science Foundation of China under Grant 31771073, Grant 61771475, and Grant 51837011; and in part by the Technology Field Foundation on Basic Strengthen Project under Grant 2019-JCJQ-JJ-096.

This work involved human subjects or animals in its research. Approval of all ethical and experimental procedures and protocols was granted by the ClinicalTrials.gov identifier under Application No. NCT00830284.

ABSTRACT Electrical impedance tomography (EIT) is a noninvasive functional diagnostic technique that has been successfully applied to human lung and brain. EIT reconstruction is an ill-conditioned problem: the regularization parameters establish a trade-off between acceptable data fitting and acceptable solution stability. This trade-off is necessary to select the optimal regularization parameters for each data frame to continuously obtain high-quality images in real-time monitoring. However, using the objective regularization parameter selection method before each image reconstruction may reduce the reconstruction efficiency, and using heuristic selection for all images may cause significant quality degradation, thereby creating challenges in long-term clinical EIT monitoring. This study explores a robust EIT target adaptive differential iterative reconstruction algorithm that does not require the advance selection of the optimal regularization parameter to facilitate the clinical application of EIT long-term bedside monitoring. Specifically, second-order Taylor approximation expansion and Euler–Lagrange theorem were used to derive the conductivity differential iteration relationship. Furthermore, the reconstruction quality and generalization ability of the proposed algorithm were validated based on comparisons with the L-curve and the generalized cross-validation parameter selection methods through simulations, phantom experiments, and human lung recruitment data. Compared with the L-curve and generalized cross-validation methods, the TADI algorithm reduces the position error by 33.07% and 47.17%, the ringing by 26.49% and 32.69%, and the shape deformation by 18.34% and 19.40% on average, respectively. The results revealed that the TADI algorithm could achieve a significant improvement over the existing state-of-the-art methods in terms of stability, consistency, and efficiency.

INDEX TERMS Electrical impedance tomography, generalized cross-validation, human lung recruitment data, L-curve validation, regularization parameters.

I. INTRODUCTION

Electrical impedance tomography (EIT) is a medical imaging technology that could be applied for a wide range of applications [1], including the early diagnosis and real-time monitoring of stroke [2], lung ventilation [3]–[5], breast cancer [6], and abdominal hemorrhage [7], among other medical conditions. In addition, the EIT can be used as a real-time monitoring device to realize the most suitable rescue opportunities for the clinical diagnosis and treatment of patients [8]. To date, the present research group has remained devoted toward the clinical application of EIT: Fu *et al.* explored and evaluated the effects of dynamic EIT on the dehydration treatment in patients with cerebral infarction [9], and Yang Bin *et al.* reported a significant negative correlation between the variations in brain impedance and intracranial pressure of patients with cerebral edema [10]. In addition, Li *et al.* explored and applied dynamic EIT to conduct

The associate editor coordinating the review of this manuscript and approving it for publication was Kumaradevan Punithakumar.

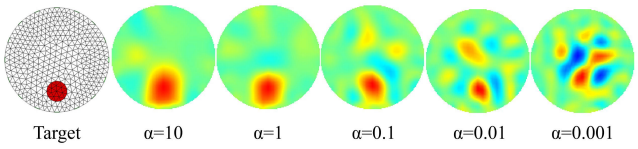

FIGURE 1. EIT images reconstructed by the damped least-squares algorithm with different regularization parameters α for the same target.

real-time monitoring of the change in electrical conductivity caused by cerebral hypoxia injury during total aortic arch replacement [11], which initially demonstrated the effectiveness of the dynamic-impedance imaging technology in such a clinical application.

A serious challenge in the EIT image reconstruction process is to surpass the ill-condition of the inverse problem [12]. The ill-conditioned characteristic is an unstable property that yields a considerable deviation between the observed and theoretical solutions in case the boundary voltage is slightly disturbed. Presently, most EIT bedside-monitoring techniques adopt the single-step damped least-squares (DLS) algorithm, which is theoretically advantageous for obtaining a high imaging speed, stable estimated solution, and strong artifact suppression, among other benefits [13]. It is essential to select the optimal regularization parameters individually for each frame of the clinical data to reasonably optimize the accuracy and robustness of the regularization solution for the practical utilization of the advantages of the damped least-squares algorithm [14]. Moreover, in serious cases, considering an unreasonable regularization parameter for the image reconstruction process can result in incorrect cognition and judgment. Fig. 1 shows the impact of using different regularization parameters α on EIT reconstruction. In this simulation, the data was generated from a single target marked in red and 0.1% random additive Gaussian white noise was added. The results demonstrate that when the regularization parameter is greater than 0.1, the target image can be reconstructed stably, but when the regularization parameter is equal to 0.001, the target image cannot be reconstructed correctly.

In particular, the optimization of the regularization parameter is vital for several image reconstruction techniques. However, current research on the selection of the regularization parameter presents its own limitations during the practical application of EIT bedside-monitoring [15]. Moreover, the regularization parameter selection criteria proposed thus far can be divided into two categories based on (i) prior information such as noise error level, and (ii) a-posteriori parameter selection criterion matching the original data with the inclusion of qualitative or quantitative information to the solution [16]. In context, the unbiased predictive risk estimator (UPRE) is a statistical estimation method based on the quadratic norm of prediction error, assuming that the error is independently and identically distributed with the knowledge of noise variance [17]. The equivalent degrees of freedom consider the linear dependency between the observed and theoretical solutions, assuming that the residual norm is a Chi-square distribution with known noise variance and degrees of freedom [18]. In addition, Morozov's discrepancy principle is a widely used method for selecting the regularization parameter by matching the residual norm to a noise-level-dependent upper limit [19]. The noise figure is derived from the ratio of output SNR to input SNR, thereby selecting the optimal regularization parameter from the signals of interest and noise levels [20]. Unlike the abovementioned methods, the L-curve validation (LCV) and generalized cross-validation (GCV) allow the selection of the regularization parameter without knowledge of the noise variance. More precisely, the LCV method considers the residual norm as the x-axis and the image norm as the y-axis to select the optimal regularization parameter by locating the corner point of the curvature. In contrast, the GCV method, which is derived from the leave-one-out principle, selects the optimal regularization parameter corresponding to the minimum error [21].

In practice, the verification of the establishment of a-priori selection criteria is challenging, which further extends their application range. Although posterior selection methods such as the LCV and GCV are reliable, they pose certain disadvantages such as a complex calculation process, inferior real-time performance, and under-regularization [22]. Moreover, all the abovementioned parameter selection methods pose a common problem: the selected regularization parameters are applicable to only the current measured voltage data, which fails to satisfy the continuous real-time dynamic imaging requirements of EIT clinical applications [23].

Presently, researchers tend to select the most appropriate regularization parameters in clinical EIT based on heuristic experience methods, which largely depends on the level of subjective experience and cannot be adjusted for various spatial resolutions and noise measurement performance [24]. This study aimed to explore a robust and dynamic EIT reconstruction algorithm without involving the prior selection of the optimal regularization parameter. This algorithm is novel as it combines the respective advantages of the differential iteration method and the damped least-squares method to facilitate the construction of an offline image reconstruction matrix that is able to retain the main signal information of the image. Furthermore, an online search solution can be employed for image reconstruction by adjusting the search step, which can effectively converge to a reasonable result. Therefore, the TADI algorithm proposed in our paper can address the EIT long-term bedside monitoring problem: objective selection methods are required to choose the optimal regularization parameter for each data frame or heuristic selection is required for all images, and may cause a significant decline in image efficiency and quality.

The remainder of this manuscript is organized as follows. The algorithm framework along with the proposed experimental setup is described in Section II, and the results of simulation, phantom experiment, and human lung recruitment data are presented in Section III. Thereafter, the advantages

and disadvantages of the algorithm including the future scope of this research are stated in Section IV. Finally, the conclusions are marked in Section V.

II. METHOD

A. ALGORITHM FRAMEWORK

1) DYNAMIC EIT

The dynamic EIT (DEIT) technology performs reconstruction imaging by calculating the normalized boundary voltage value in a short time interval (t_1, t_2) to inversely estimate the normalized conductivity change distribution. As a popular differential imaging method, DEIT can significantly diminish the influence of modeling errors and instrument noise [25].

With the slight change in the conductivity distribution, the DEIT forward problem model can be linearized as

$$\Delta z = \boldsymbol{S}\Delta\boldsymbol{\rho} + \boldsymbol{e}, \tag{1}$$

where $\Delta\boldsymbol{\rho} \in \mathbb{R}^{N\times 1}$ and $\boldsymbol{S} \in \mathbb{R}^{M\times N}$ (N and M denote the number of elements and measurements, respectively) denote the distribution matrix of normalized conductivity change in the time interval (t_1, t_2) and the approximate linearization sensitivity matrix, respectively; the matrix $\boldsymbol{e} \in \mathbb{R}^{M\times 1}$ represents the additive noise or error. $\Delta z \in \mathbb{R}^{M\times 1}$ denotes the normalized voltage change matrix defined as

$$\Delta z = \frac{\boldsymbol{v}_2 - \boldsymbol{v}_{Ref}}{\boldsymbol{v}_{Ref}}, \tag{2}$$

where $\boldsymbol{v}_{Ref} \in \mathbb{R}^{M\times 1}$ and $\boldsymbol{v}_2 \in \mathbb{R}^{M\times 1}$ represent the vectors containing all the measurement values of the boundary voltage at times t_1 and t_2, respectively.

The DLS algorithm defined the cost function $\boldsymbol{J}$ as

$$\begin{aligned}\min_{\Delta\boldsymbol{\rho}} \boldsymbol{J} &= \|\Delta z - \boldsymbol{S}\Delta\boldsymbol{\rho}\|_2^2 + \alpha\,\|\boldsymbol{L}\Delta\boldsymbol{\rho}\|_2^2 \\ &= [\Delta z - \boldsymbol{S}\Delta\boldsymbol{\rho}]^T[\Delta z - \boldsymbol{S}\Delta\boldsymbol{\rho}] + \alpha\Delta\boldsymbol{\rho}^T\boldsymbol{L}^T\boldsymbol{L}\Delta\boldsymbol{\rho},\end{aligned} \tag{3}$$

where α and $\boldsymbol{L}$ denote the regularization parameter and the weighing matrix, respectively. In addition, the consideration of the partial derivative of the cost function $\boldsymbol{J}$ to $\Delta\boldsymbol{\rho}$ equals zero and yields the minimum value of the cost function as[26]:

$$\begin{aligned}\Delta\hat{\boldsymbol{\rho}} &= [\boldsymbol{S}^T\boldsymbol{S} + \alpha\boldsymbol{R}]^{-1}\boldsymbol{S}^T\Delta z \\ &= \boldsymbol{B}\Delta z,\end{aligned} \tag{4}$$

where $\boldsymbol{R} = \boldsymbol{L}^T\boldsymbol{L}$ denotes the regularization matrix that can improve the condition number of the ill-conditioned inverse problem, including the identity matrix and NOSER prior matrix [27].

The ill-condition of (4) was further analyzed based on an alternative form of the DLS algorithm solution obtained via singular value decomposition (SVD) as

$$\Delta\hat{\boldsymbol{\rho}}_{DLS} = \sum_{i=1}^{N} \frac{\lambda_i^2}{\lambda_i^2 + \alpha l_i^2}\frac{\boldsymbol{U}_i^T\Delta z}{\lambda_i}\boldsymbol{V}_i, \tag{5}$$

where N is the rank of the sensitivity matrix $\boldsymbol{S}$, $\boldsymbol{U} \in \mathbb{R}^{m\times m}$ and $\boldsymbol{V} \in \mathbb{R}^{n\times n}$ is the left and right singular matrices for SVD, and $\lambda_i^2/(\lambda_i^2 + \alpha l_i^2)$ represents the filter factor (λ_i, λ_i^2, and αl_i^2 indicate the singular value, signal power, and noise power of the i^{th} component in the SVD subspace, respectively). Compared to the truncated SVD and LS algorithms, the DLS algorithm utilizes the regularization parameters to apply a damping effect on the high-order singular values corresponding to the rapidly varying information in the space, thus inducing greater stability in the regularization solution [28].

2) ALGORITHM IMPLEMENTATION

In this study, we propose a target adaptive differential iterative algorithm (TADI). The proposed algorithm updates the distribution of normalized conductivity change via differential iterations to obtain a stable solution. Additionally, second-order Taylor approximation expansion and Euler–Lagrange theorem were introduced to derive the differential iterative relationship of conductivity in the small region of the estimated value, and consequently achieve high-quality and rapid image reconstruction without adjusting the regularization parameters. More precisely, the estimated value of the normalized conductivity change distribution can be directly solved if α_{opt} is assumed as the optimal regularization parameter obtained by the objective selection method.

$$\Delta\hat{\boldsymbol{\rho}} = [\boldsymbol{S}^T\boldsymbol{S} + \alpha_{\text{opt}}\boldsymbol{R}]^{-1}\boldsymbol{S}^T\Delta z. \tag{6}$$

However, the selection of the optimal value α_{opt} is challenging. As can be observed from (5), a large regularization parameter that retains the contribution of the primary low-order variation information to the estimated parameter such as $\alpha_{\text{L}} = 1$ can be set to replace α_{opt}. Therefore, $\Delta\hat{\boldsymbol{\rho}}$ can be expressed as

$$\begin{aligned}\Delta\hat{\boldsymbol{\rho}} &= [\boldsymbol{S}^T\boldsymbol{S} + \alpha_{\text{L}}\boldsymbol{R}]^{-1}\boldsymbol{S}^T\Delta z + \boldsymbol{\varepsilon}^{(1)} \\ &= \boldsymbol{B}_{\text{L}}\Delta z + \boldsymbol{\varepsilon}^{(1)} = \Delta\hat{\boldsymbol{\rho}}^{(1)} + \boldsymbol{\varepsilon}^{(1)},\end{aligned} \tag{7}$$

where $\boldsymbol{B}_L = [\boldsymbol{S}^T\boldsymbol{S} + \alpha_{\text{L}}\boldsymbol{R}]^{-1}\boldsymbol{S}^T$ denotes a reconstruction matrix and $\boldsymbol{\varepsilon}^{(1)}$ represents the reconstruction error caused by the large regularization parameter α_{L} in the first iteration.

Let $f(\Delta\boldsymbol{\rho}) = \|\Delta z - \boldsymbol{S}\Delta\boldsymbol{\rho}\|_2^2$, then, $f(\Delta\boldsymbol{\rho})$ at $\Delta\boldsymbol{\rho} = \Delta\hat{\boldsymbol{\rho}}^{(k)}$ (conductivity updates of k-th iteration) can be expanded using the second-order Taylor formula to approximate:

$$\begin{aligned}\tilde{f}(\Delta\hat{\boldsymbol{\rho}}) = f(\Delta\hat{\boldsymbol{\rho}}^{(k)}) &+ \frac{\partial f(\Delta\hat{\boldsymbol{\rho}}^{(k)})}{\partial(\Delta\boldsymbol{\rho})}(\Delta\hat{\boldsymbol{\rho}} - \Delta\hat{\boldsymbol{\rho}}^{(k)}) \\ &+ \frac{1}{2}(\Delta\hat{\boldsymbol{\rho}} - \Delta\hat{\boldsymbol{\rho}}^{(k)})^T\frac{\partial^2 f(\Delta\hat{\boldsymbol{\rho}}^{(k)})}{\partial(\Delta\boldsymbol{\rho})^2}(\Delta\hat{\boldsymbol{\rho}} - \Delta\hat{\boldsymbol{\rho}}^{(k)}) \\ &+ R_n(\Delta\hat{\boldsymbol{\rho}}^{(k)}).\end{aligned} \tag{8}$$

Based on the Euler–Lagrange method to determine the extreme value of the approximate function $\tilde{f}(\Delta\hat{\boldsymbol{\rho}})$,

$$\begin{aligned}&\frac{\partial\tilde{f}(\Delta\hat{\boldsymbol{\rho}}^{(k+1)})}{\partial(\Delta\boldsymbol{\rho})} \\ &\quad= \frac{\partial f(\Delta\hat{\boldsymbol{\rho}}^{(k)})}{\partial(\Delta\boldsymbol{\rho})} + (\Delta\hat{\boldsymbol{\rho}}^{(k+1)} - \Delta\hat{\boldsymbol{\rho}}^{(k)})^T\frac{\partial^2 f(\Delta\hat{\boldsymbol{\rho}}^{(k)})}{\partial(\Delta\boldsymbol{\rho})^2}.\end{aligned} \tag{9}$$

In the iterative reconstruction, the direct utilization of $\boldsymbol{S}^T\boldsymbol{S}$ as the Hessian matrix increases the ill-condition of each iteration [29]. Consequently, the meaning cannot be extracted from the reconstruction result owing to the amplification and accumulation of the measurement errors. Moreover, the inclusion of the regularization term $\alpha_{\mathrm{L}}\boldsymbol{R}$ to compensate the unreliable component of the measurement, corresponding to the small singular value in $\boldsymbol{S}^T\boldsymbol{S}$, causes the $(\boldsymbol{S}^T\boldsymbol{S}+\alpha_{\mathrm{L}}\boldsymbol{R})$ diagonal to be dominant and the elements to be positive for sufficiently large values of α_{L}. Furthermore, the positive definite nature of the matrix is significantly improved the ill-conditioned matrix inverse problem apart from simplifying the calculation of high-order derivatives of the Hessian matrix. Thus, Eq. (9) can be deduced as

$$\Delta\hat{\boldsymbol{\rho}}^{(k+1)} = \Delta\hat{\boldsymbol{\rho}}^{(k)} - \left(\frac{\partial^2 f(\Delta\hat{\boldsymbol{\rho}}^{(k)})}{\partial(\Delta\boldsymbol{\rho})^2}\right)^{-1}\frac{\partial f(\Delta\hat{\boldsymbol{\rho}}^{(k)})}{\partial(\Delta\boldsymbol{\rho})}, \quad (10)$$

As $\Delta\boldsymbol{z} - \boldsymbol{S}\Delta\hat{\boldsymbol{\rho}}$ approaches 0, the disturbance is located in the linear approximation region and the sensitivity matrix $\boldsymbol{S}$ need not be recalculated. The iterative formula of the final solution can be expressed as

$$\Delta\hat{\boldsymbol{\rho}}^{(k+1)} = \Delta\hat{\boldsymbol{\rho}}^{(k)} + \boldsymbol{B}_{\mathrm{L}}[\Delta\boldsymbol{z} - \boldsymbol{S}\Delta\hat{\boldsymbol{\rho}}^{(k)}], \quad (11)$$

where $\Delta\hat{\boldsymbol{\rho}}^{(0)} = [\boldsymbol{S}^T\boldsymbol{S} + \alpha_{\mathrm{L}}\boldsymbol{R}]^{-1}\boldsymbol{S}^T\Delta\boldsymbol{z}$ represents the initial estimated value of the normalized conductivity change distribution. This iteration can be terminated by setting the threshold of the change to $\left\|\Delta\boldsymbol{\rho}^{(k+1)} - \Delta\boldsymbol{\rho}^{(k)}\right\|^2 < \delta, \delta \ll 1$ or limiting the maximum number of iterations to $k_{\max}$.

In this iterative process, the deviation between the estimated and measured voltage was processed based on the initial smooth-estimated value of the normalized conductivity change distribution. To determine the various governing factors in the reconstruction of the EIT target, the algorithm retains the contribution of the fundamental low-order variation information toward the reconstruction parameters to reduce the condition number in each iteration. Thus, the variation between the estimated and real values decreased continuously after each iteration, and a target reconstructed image was obtained with improved quality.

Subsequently, the sensitivity and regularization matrices were usually determined for a given reconstruction model template, and accordingly, the iterative reconstruction matrix $\boldsymbol{B}_{\mathrm{L}}$ was determined after setting the large regularization parameter α_L. The reconstructed image was obtained via the following steps:

Step 1: Solve the forward model including the disturbance target to obtain the boundary voltage data $\boldsymbol{v}$ containing the measurement noise and calculate the normalized voltage value $\Delta\boldsymbol{z}$.

Step 2: Determine the corresponding Jacobian matrix $\boldsymbol{J}$ and regularization matrix $\boldsymbol{L}^T\boldsymbol{L}$ based on the given reconstruction model template, and subsequently, derive the iterative reconstruction matrix $\boldsymbol{B}_{\mathrm{L}}$ based on the initial large regularization parameters α_{L} without any selection.

Step 3: Calculate the initial iteration value $\Delta\hat{\boldsymbol{\rho}}^{(0)} = \boldsymbol{B}_{\mathrm{L}}\Delta\boldsymbol{z}$ using the DLS algorithm. The optimization iterative calculation was performed along with (11) to obtain a target that more closely represents the real disturbance target.

Step 4: Terminate the iteration upon satisfying the condition and obtain the EIT normalized conductivity change distribution image.

3) REGULARIZATION PARAMETER SELECTION

According to the regularization principle, the selection of the optimal regularization parameters can optimize the perturbation and errors in the regularization solution [30]. Prior research reported that LCV, GCV, and UPRE achieve comparable results for the simulation data [31]. As UPRE requires prior information regarding noise, LCV and GCV were selected as the comparison methods in this study.

Among these methods, the LCV method is the most commonly used method for objective selection of a regularization parameter in ill-conditioned inverse problems [32]. In addition, a regularization parameter curve can be fitted, considering the logarithms of the residual norm and image norm as the x- and y-axis, respectively. As the shape of the coordinate drawn with $(\lg\left\|\boldsymbol{S}\Delta\boldsymbol{\rho}_\alpha - \Delta\boldsymbol{z}\right\|, \lg\left\|\Delta\boldsymbol{\rho}_\alpha\right\|)$ depicts the letter "L", it is called the L-curve method. In particular, the primary function of the LCV method is locating the maximum value of the curvature and selecting it as the optimal regularization parameter [33]. This method demonstrates the characteristics of displaying an evident variation in the function image and improved applicability. In certain cases, an inaccurate inflection point was obtained by the curve, which caused failure in obtaining the corresponding optimal regularization parameters.

The GCV method considers that if any element in the measured value was discarded, the corresponding regularization solution should be able to accurately predict the discarded value. The GCV function is expressed as

$$G(\lambda) = \frac{\left\|\boldsymbol{S}\Delta\boldsymbol{\rho}_\alpha - \Delta\boldsymbol{v}\right\|_2^2}{(\mathrm{trace}(\boldsymbol{I} - \boldsymbol{S}\boldsymbol{B}_\alpha))^2}, \quad (12)$$

where $B_\alpha = \left(\boldsymbol{S}^{\mathrm{T}}\boldsymbol{S} + \alpha\boldsymbol{R}\right)^{-1}\boldsymbol{S}^{\mathrm{T}}$ and the trace() function calculates the sum of the main diagonal elements of the matrix in the brackets. The minimum error corresponds to the optimal regularization parameter under this criterion. However, the regularization parameters obtained by this method yielded an under-regularized solution, which prominently increased the image noise.

As stated earlier, the proposed differential iterative algorithm does not require prior information regarding noise. First, the estimated value $\Delta\hat{\boldsymbol{\rho}}_{TADI}$ of the normalized conductivity change distribution was obtained using the TADI algorithm, which can be evaluated using a single-step DLS algorithm with the optimal regularization parameter expressed as

$$\Delta\hat{\boldsymbol{\rho}}_{TADI} = (\boldsymbol{S}^T\boldsymbol{S} + \alpha\boldsymbol{R})^{-1}\boldsymbol{S}^T\Delta\boldsymbol{z}. \quad (13)$$

Moreover, all the parameters in (16) are known, except the regularization parameter α. The corresponding regularization parameters can be obtained by minimizing the vector space distance on both sides of the equation with Euclidean norm

$$\hat{\alpha} = \arg\min_{\alpha} \left\| (\boldsymbol{S}^T \boldsymbol{S} + \alpha \boldsymbol{R})^{-1} \boldsymbol{S}^T \Delta z - \Delta \hat{\boldsymbol{\rho}}_{TADI} \right\|_2. \quad (14)$$

Combined with (11), the function for selecting the optimal regularization parameter of differential iterations can be defined as

$$TADI(\alpha) = \left\| \boldsymbol{A} + \alpha \boldsymbol{R} \Delta \hat{\boldsymbol{\rho}}_{TADI} \right\|_2, \quad (15)$$

where $\boldsymbol{A} = \boldsymbol{S}^T (\boldsymbol{S} \Delta \hat{\boldsymbol{\rho}}_{TADI} - \Delta z)$ represents a deterministic matrix, the optimal regularization parameters were obtained by minimizing (15).

B. EXPERIMENTAL FRAMEWORK

1) PERFORMANCE METRICS

In this study, a set of criteria was designed to characterize the performance of the proposed algorithm. These criteria included the GREIT consensus evaluation methodology proposed by Adler *et al.*, which is a broadly accepted methodology in this field [34]. In addition, a quarter of the maximum conductivity change occurring in the reconstructed image was considered as the reference amplitude, and the element amplitude larger than the reference amplitude was considered as the region of perturbation (ROP). Moreover, the figures of merit included the position error (PE), resolution (RES), shape deformation (SD), and ringing (RNG) as the criteria. To compare the performance metric of each method, the ROP was normalized to the region of interest (ROI) in the calculation.

(i) The PE indicated the position deviation of the reconstructed target obtained by evaluating the distance between the centers of reconstruction and the simulation targets as

$$PE = d_{REAL} - d_{ROP}, \quad (16)$$

where d_{REAL} and d_{ROP} denote the distance of the medium center from the simulation target gravity center and the reconstruction target gravity center, respectively. Furthermore, PE should be as close to zero as possible and uniform for targets at various radial positions.

(ii) The RES signified the shape of the target conductivity distribution obtained by determining the percentage of the disturbance reconstruction target area A_{ROP} in the entire reconstruction medium area A. In particular, the RES ought to be small and uniform for a more accurate reconstruction.

$$RES = \sqrt{\frac{A_{ROP}}{A}} \quad (17)$$

(iii) The SD measured the fraction of the reconstructed target not fitting within the equal area. The small and uniform SD value indicated that the reconstructed image rarely displayed irregular-shaped artifacts surrounding the target area.

$$\mathrm{SD} = \frac{A_C}{A_{ROP}}, \quad (18)$$

where A_C represents the total area within the ROP, and not within the simulation target area.

(iv) The RNG represented the over-extending degree of the opposite sign around the reconstructed target area. Moreover, a small and uniform RNG value indicates the small size of the artifacts around the reconstructed target and can cause incorrect interpretation.

$$\mathrm{RNG} = \frac{A_O}{A_{ROP}}, \quad (19)$$

where A_O represents the total area outside the ROP, when the direction of the reconstructed normalized conductivity change was opposite to that of the simulation target.

2) SIMULATION EXPERIMENTS

In the experiment to determine the regularization parameter selection, the radius of each model was set to 10 cm. The circular disturbance target with a radius of 1 cm and conductivity of 1.5 S/m was placed at the radial distances of 0 cm, 2.5 cm, 5 cm, and 7.5 cm from the center toward the boundary. Referred to the noise range of simulation setting in the literature [35], [36], the additive Gaussian white noise that increased gradually from 0.1% to 0.8% was included in the boundary voltage data in this experiment. The statistical significance for the experimental process of regularization parameters selection was ensured by randomly simulating each noise for 50 instances, and the results were compared in the form of mean $\pm$ standard deviation.

In the image simulation experiment, the proposed algorithm was compared to the reconstructed image obtained using the one-step DLS algorithm. The regularization parameter was selected using the LCV and GCV methods to verify the effectiveness and robustness of the proposed reconstruction algorithm. Unless specified, the parameter of the TADI algorithm was set to $\delta = 0.1$, $\alpha_{\mathrm{L}} = 1$ and $\boldsymbol{R} = diag(\boldsymbol{S}^T \boldsymbol{S})$, a total of 1024 elements were obtained using the finite element model for inverse model. There were 16 electrodes with adjacent current stimulation (amplitude: 1 mA, frequency: 50 kHz) and adjacent voltage measurement pattern on the surface.

The single disturbance target simulation experiment was conducted to study the influence of the alternating target and electrode positions, including the target size variation for the images reconstructed using the three methods. The conductivity of background was uniform with the amplitude 1 S/m. The conductivity of the positive disturbance target was 1.5 S/m. In simulation 1, we used a single positive disturbance target with the conductivity of 1.5 S/m and the radius of 1 cm at (−0.43, −0.97), (−1.43, 1.60), (3.06, 0.98), (−3.72, −5.24). In simulation 2, we used a single positive disturbance target located at (0, −5) with the different radii of 1.00 cm, 1.33 cm, 1.67 cm, and 2.00 cm. Then we placed a positive disturbance target with the radius of 1 cm at (−3, −5.5), and a negative disturbance target with the radius of 1 cm at (0, −6.5) to compare the reconstruction images of various conductivity and electrode

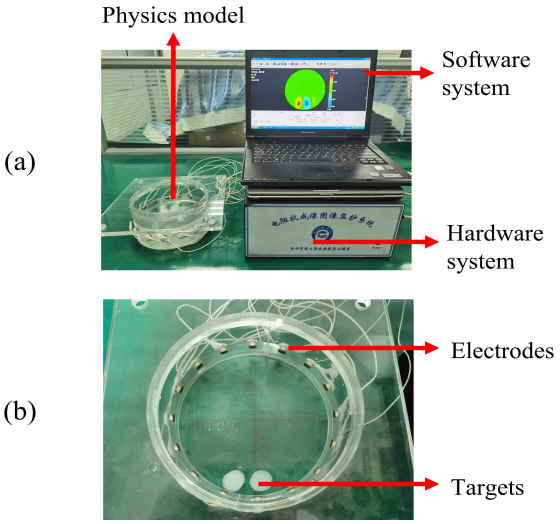

FIGURE 2. Phantom experiment platform. (a) EIT experiment platform in our laboratory, including the software system, hardware system, and phantom model. (b) Cylindrical phantom tank (diameter: 17 cm) filled with saturated calcium sulfate solution; electrodes were 3 cm in height and 1 cm in diameter. Cylindrical blocks of agarose were placed as disturbance targets whose conductivity was measured using a four-electrode measurement box.

configurations. And the robustness of the proposed algorithm for complex models was further verified by setting up human lung (length: 30 cm, width: 20 cm) experiment. In all image results, the red and blue in the color bar represent the increase and decrease of normalized conductivity change, respectively [23].

In all the image simulation experiments, 0.1% random Gaussian white noise was added to the boundary voltage data, and the final image reconstruction results were obtained by calculating the average value for 20 instances. All simulation evaluation periods were determined on a computer with a CPU operating at 3.20 GHz with 64 GB RAM.

3) PHANTOM EXPERIMENT

Based on the simulation experiments, a phantom experiment was set up to verify the robustness and effectiveness of the TADI algorithm. The EIT experiment platform constructed in our research laboratory is presented in Fig. 2. The original boundary voltage data were collected using a FMMU-EIT5, which uses the polar current injection and adjacent voltage measurement pattern with 16 equidistant electrodes. In addition, the stimulation current was set with an amplitude of 1 mA and a frequency of 50 kHz.

The saturated calcium sulfate solution with a conductivity of 0.24 S/m was injected into a cylindrical tank at room temperature. The self-produced cylindrical agarose blocks of 4 cm height were used to represent the corresponding positive and negative disturbance targets. Moreover, the image reconstruction quality obtained from these three methods was compared to the volume or normalized conductivity change, and the results were quantified based on the resolution metric.

4) HUMAN LUNG RECRUITMENT DATA

The EIT technology can provide real-time bedside guidance for operating the mechanical ventilation by extracting the regional indicators of potential lung injury [37], [38]. We used the real EIT clinical data acquired from a patient on Primary ARDS triggered by parainfluenza pneumonia undergoing progressive lung recruitment and performed positive end-expiratory pressure (PEEP) titration to further verify the effectiveness and robustness of the TADI algorithm in clinical monitoring [39], [40].

III. RESULTS

A. REGULATION PARAMETER SELECTION

The results of the three objective regularization parameter selection methods applied to various locations of disturbance targets are presented in Fig. 3. The regularization parameters increased with the noise level, which was consistent with the definition of the regularization parameters. For the same regularization matrix, the filtering ability of the filter factor was stronger for the high-order signal variation and the influence of the error on image reconstruction diminished more effectively under a larger regularization parameter. When the disturbance target was placed at the center of the circular region, the selection results of the TADI and LCV methods improved slightly, and the fluctuation range remained small, regardless of the constant increase in the noise level. Although the selection results of the GCV method remained within a reasonable range, these results fluctuated broadly and did not exhibit sufficient stability in the simulation process.

Moreover, the sensitivity of the conductivity increased as the disturbance target approached the boundary, and the three selection methods delivered relatively similar performances. Similar to the GCV method, the TADI method utilized the residual norm fitting to select the parameters, but it still maintained high robustness in all the above-mentioned cases.

B. IMAGE RECONSTRUCTION

Fig. 4 and 5 depict the results of single disturbance target reconstruction based on three reconstruction methods Fig. 4(a) indicates that in comparison with alternative methods, the size and shape of the disturbance targets reconstructed by the TADI algorithm were closer to the model with lesser number of reconstruction artifacts and relatively higher quality images were obtained. The reconstruction performance of the three methods is presented in Fig. 4(b). Compared with the LCV and GCV methods, the TADI algorithm reduced the PE by 36.92% and 45.25%, the RNG by 15.73% and 28.59%, and the SD by 10.95% and 21.73% on average, respectively. Thus, the results of the TADI algorithm were considerably superior than the two alternative methods when the disturbance target was placed at the center. Furthermore, as the disturbance target moved closer to the boundary, the gap between the image RES reconstructed by

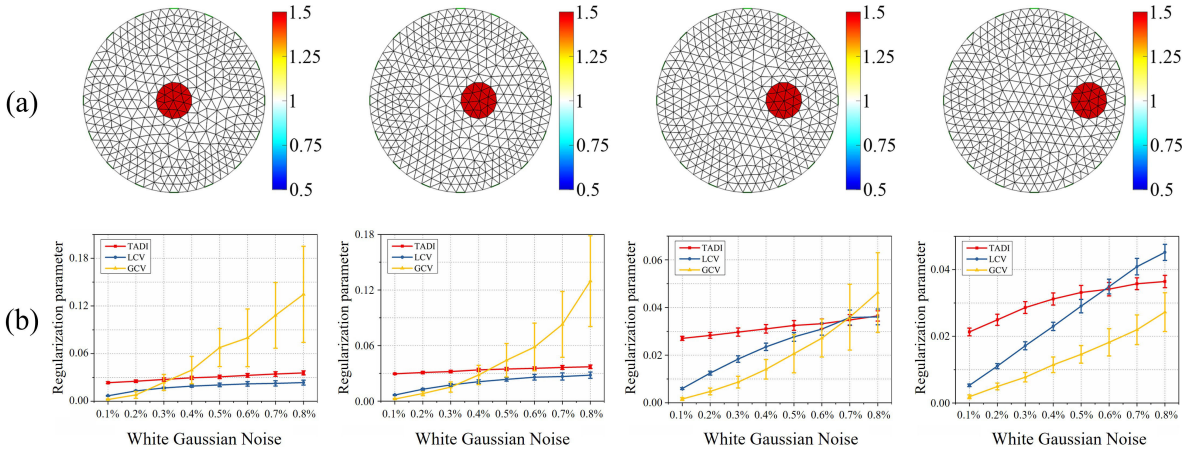

FIGURE 3. Regularization parameter selection results. (a) Simulation models of regularization parameter selection experiments. (b) Regularization parameter selection results from three methods for the disturbance target location presented in Fig. 3(a).

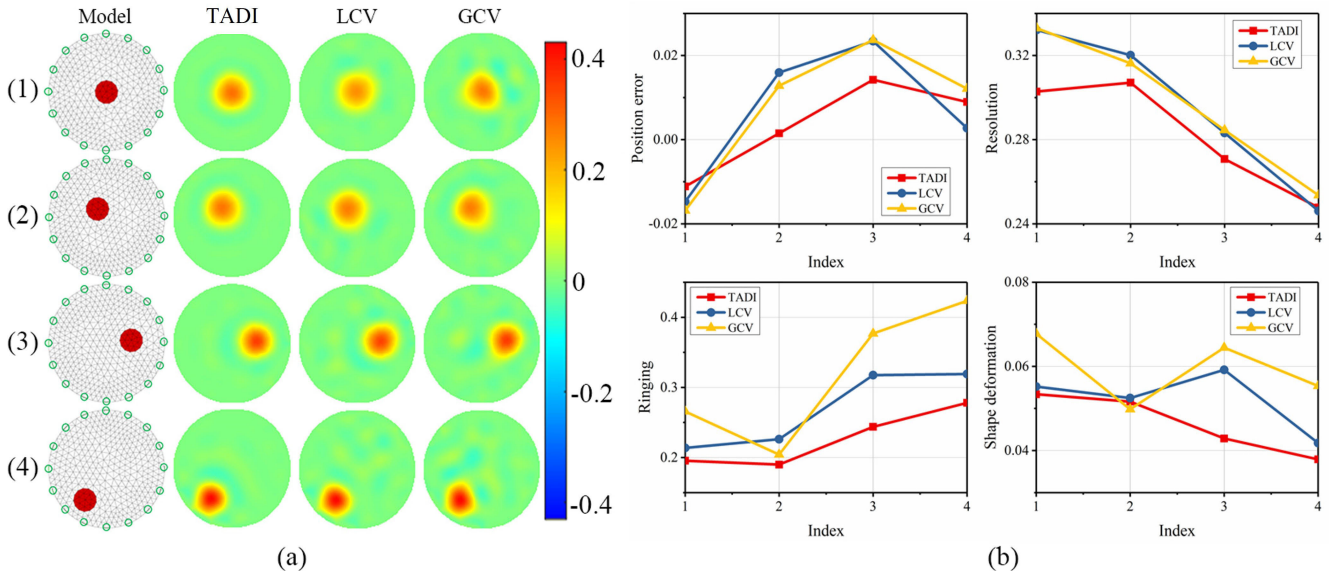

FIGURE 4. Single-disturbance target reconstruction simulation experiment results. (a) Positive disturbance targets at various positions were reconstructed based on three reconstruction methods. (b) Performance figures of merit obtained from the reconstructed image in Fig. 4(a), including PE, RES, RNG, and SD. The temporal response of the TADI, LCV, and GCV methods required 34.77 ± 1.66 ms, 1415.04 ± 17.34 ms, and 1,370.37 ± 17.52 ms for each image reconstruction, respectively.

each method becomes narrow. Regardless, the TADI algorithm outperformed the two alternative methods in most cases.

As can be observed from Fig. 5(a), the TADI algorithm could more clearly reconstruct the smaller disturbance targets. Moreover, the number of artifacts around the disturbance target image reconstructed using the TADI algorithm reduced significantly as the radius of the disturbance target increased. The reconstruction performance of the three methods is presented in Fig. 5(b). Compared with the LCV and GCV methods, the TADI algorithm reduced the PE by 29.81% and 48.55%, the RNG by 35.56% and 36.71%, and the SD by 24.02% and 17.17%, on average, respectively. As observed, the performance of the TADI algorithm was superior to that of the two alternative methods, which was consistent with the reconstructed images in Fig. 5(a).

Fig. 6 and 7 illustrate that the TADI algorithm can reconstruct a more stable and accurate image in the double disturbance target reconstruction simulation experiment, irrespective of any variations in the current stimulation pattern or the disturbance target conductivity. Compared with the single disturbance target, the RES metric calculation of the double disturbance targets is the same, and is obtained by determining the percentage of the disturbance reconstruction target area, A_{ROP}, in the entire reconstruction medium area A. However, due to the bidirectional disturbance, the target consists of one positive conductivity and one negativity conductivity disturbance target, the disturbance reconstruction target area

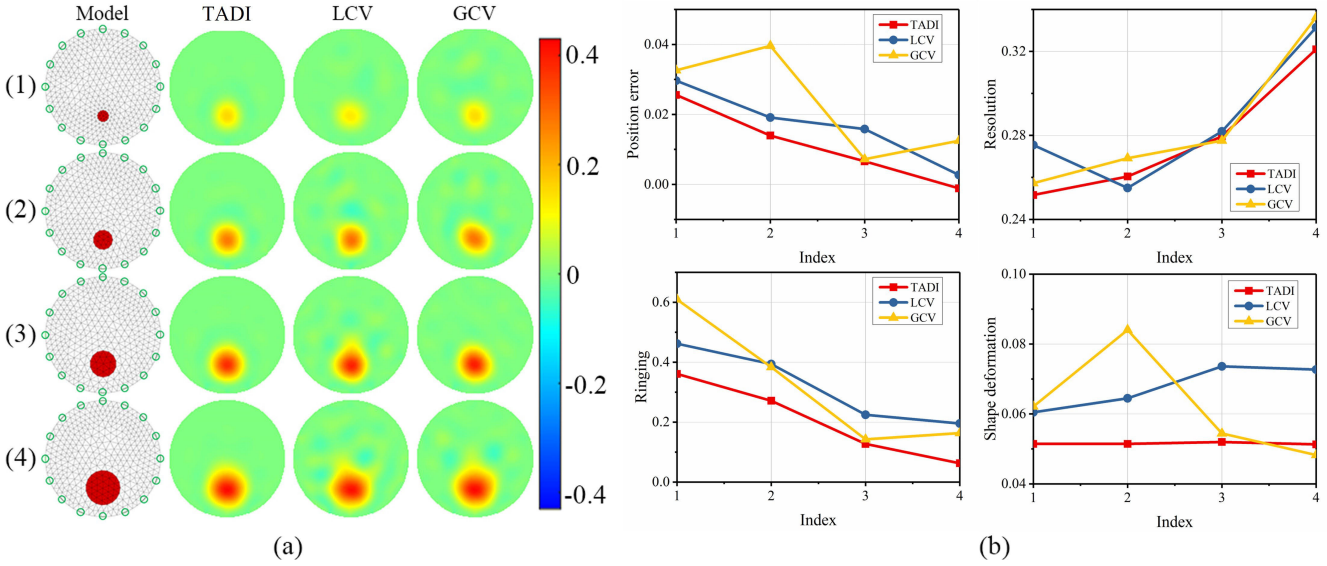

FIGURE 5. Single-disturbance target reconstruction simulation experiment results. (a) Positive disturbance targets with varying radii were reconstructed based on three reconstruction methods. (b) Performance figures of merit obtained by reconstructing the images in Fig. 5(a), including PE, RES, RNG, and SD. The temporal response of the TADI, LCV, and GCV methods required 35.00 ± 1.89 ms, 1424.41 ± 18.47 ms, and 1385.16 ± 19.03 ms for each image reconstruction, respectively.

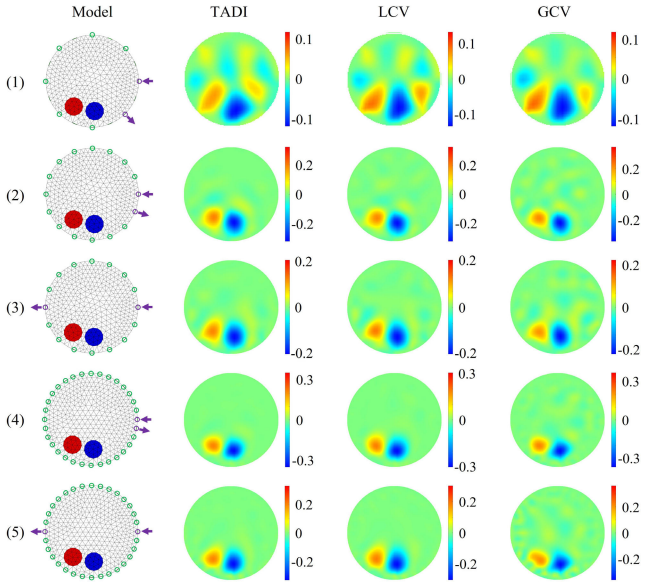

FIGURE 6. Simulation results of reconstructing double disturbance targets with four stimulation patterns. (1) 8 electrodes with adjacent current stimulation; (2) 16 electrodes with adjacent current stimulation; (3) 16 electrodes with polar current stimulation; (4) 32 electrodes with adjacent current stimulation; (5) 32 electrodes with polar current stimulation. All models use adjacent voltage measurement pattern. The conductivity of bidirectional disturbance targets were 1.5 S/m and 0.5 S/m, and the radius of each target was 1 cm.

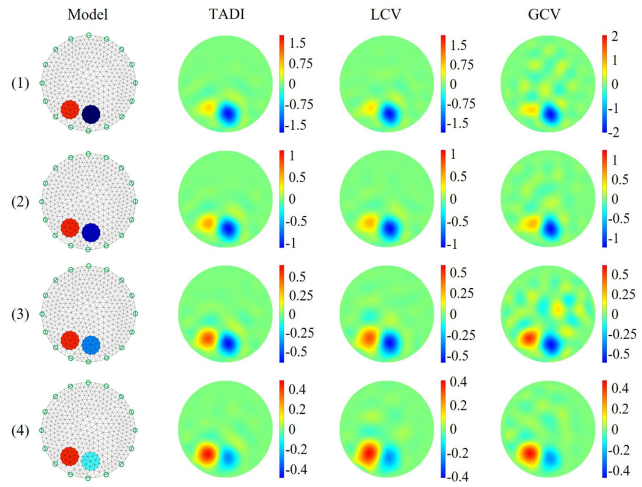

FIGURE 7. Simulation results of reconstructing double disturbance targets with various conductivities. The conductivity and radius of each positive target was 1.5 S/m and 1 cm, whereas those of each negative target was (1) 0.2 S/m and 1 cm; (2) 0.4 S/m and 1 cm; (3) 0.6 S/m and 1 cm; (4) 0.8 S/m and 1 cm. All models use 16 electrodes with adjacent current stimulation and adjacent voltage measurement pattern. The temporal response of the TADI, LCV, and GCV methods required 34.17 ± 0.72 ms, 1,390.67 ± 19.13 ms, and 1,378.32 ± 19.74 ms for each image reconstruction, respectively.

A_{ROP} was calculated by the conductivity amplitude absolute value.

In Fig. 8(1) and (2) represent the double lungs reconstruction and (3) the single lung reconstruction. As can be observed from the results, the TADI algorithm could more accurately reconstruct the position, size, and shape of the target. In contrast, the images reconstructed using the LCV and GCV methods contained large artifacts and deformed targets.

In summary, compared with the LCV and GCV methods, the TADI algorithm reduced the PE by 33.07% and 47.17%, the RNG by 26.49% and 32.69%, and the SD by 18.34% and 19.40% in simulation experiments on average, respectively. The results revealed that the TADI algorithm was more

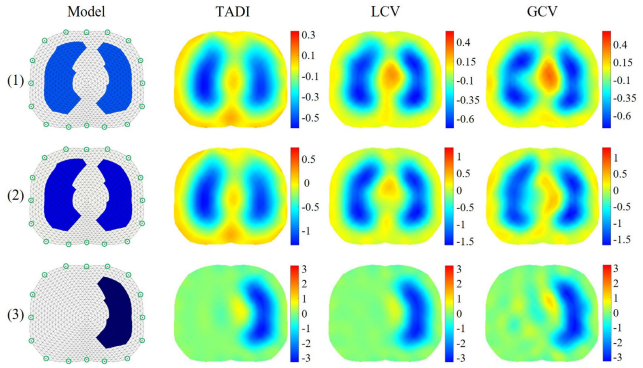

FIGURE 8. Simulation results of human lung reconstruction. The conductivity of the background (white) was 0.2 S/m and that of lung (blue) was (1) 0.18 S/m; (2) 0.16 S/m; (3) 0.14 S/m. All models used 16 electrodes with adjacent current stimulation and adjacent voltage measurement pattern. The temporal response of the TADI, LCV, and GCV methods required 16.13 ± 0.17 ms, 1312.82 ± 18.91 ms, and 1270.32 ± 19.43 ms for each image reconstruction, respectively.

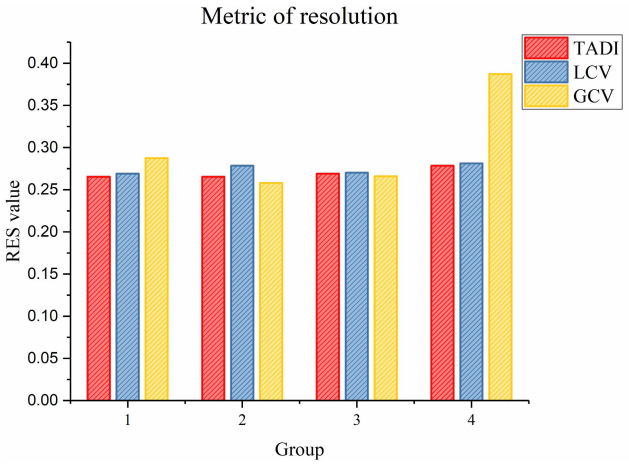

FIGURE 10. Resolution histogram of the phantom experiment reflecting the reconstruction quality of the three reconstruction methods shown in Fig. 9.

TABLE 1. Various cylindrical blocks of agarose in phantom experiment.

	Group	1	2	3	4
Positive Target	Volume (ml)	12.56	12.56	12.56	12.56
	Conductivity (S/m)	0.36	0.36	0.36	0.36
Negative Target	Volume (ml)	12.56	12.56	12.56	12.56
	Conductivity (S/m)	0.16	0.12	0.08	0.04

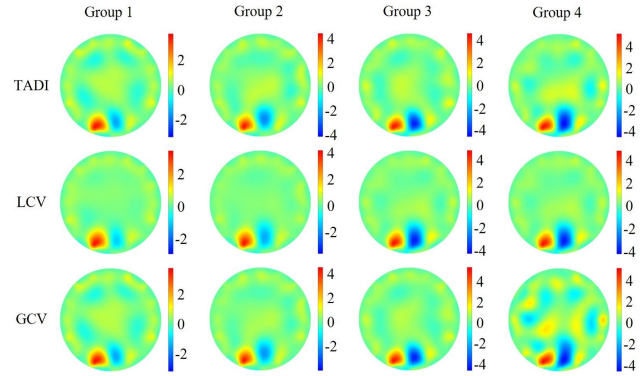

FIGURE 9. Results of phantom experiment: blocks of agarose disturbance targets were reconstructed based on three methods as listed in Table 1. All models used 16 electrodes with polar current stimulation and adjacent voltage measurement pattern. The temporal response of the TADI, LCV, and GCV methods required 14.96 ± 0.61 ms, 1420.58 ± 18.70 ms, and 1396.77 ± 19.41 ms for each image reconstruction, respectively.

effective and robust than the two alternative methods in the simulation experiments.

C. PHANTOM EXPERIMENT

The specific conditions of disturbance targets in the phantom experiment are listed in Table 1. In each group, a frame of stable data was selected for the three methods of reconstruction imaging.

Fig. 9 depicts the reconstruction results of the double blocks of agarose disturbance targets in the tank, based on the three reconstruction methods. As the conductivity of the negative disturbance target gradually decreased, the TADI algorithm maintained robustness and resolution and could clearly distinguish the two disturbance targets in all the cases. However, the quality of the image reconstructed by the LCV method was poor when the conductivities of the disturbance target and background was similar (group 1). As the conductivity of the disturbance target varied significantly, the images reconstructed by the GCV method contained large artifacts and deformed targets (group 4). The analysis of the reconstructed image RES metric is presented in Fig. 10, which was consistent with the results depicted in Fig. 9. Thus, the effectiveness and robustness of the proposed algorithm were verified for the phantom experiment.

D. HUMAN LUNG RECRUITMENT DATA

Fig. 11 depicts a typical series of tidal breath EIT differential reconstructed images of a patient with ARDS during a lung recruitment maneuver followed by PEEP titration. The bottom colormap applies to all images and represents normalized impedance increases (blue) and decreases (red) relative to an average peak-expiratory reference image.

The EIT image of a typical tidal breath in the lung reconstructed using the three methods is presented in Fig. 11(a), wherein the image of the peak expiratory value is marked with the red rectangle, corresponding to the condition of low lung gas and low impedance value. In addition, the purple rectangle indicates the image of peak inspirations in this breath, wherein the blue lung-shaped area indicates the increased impedance caused by the presence of more volume of air in the lungs.

Fig. 11(a) clearly portrays that the shape reconstructed by the TADI algorithm was more uniform with less amount of unexplained deformation in all the cases, compared with those obtained by the two alternative methods. Moreover, the intra-tidal difference image obtained by subtracting the

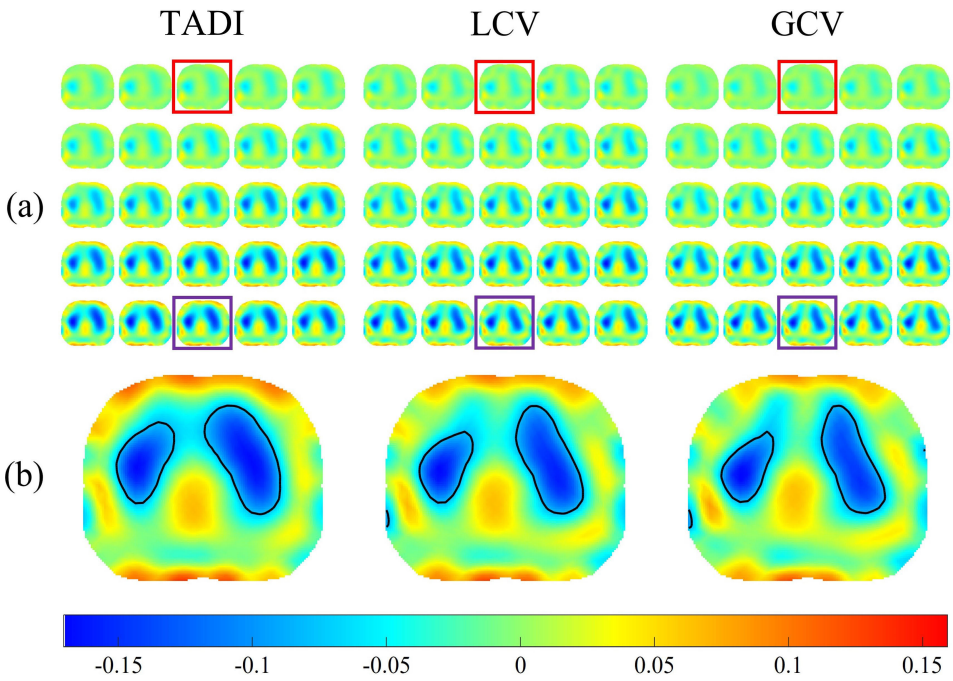

FIGURE 11. EIT differential reconstructed images of typical tidal breath in patients with acute respiratory distress syndrome. Images represent the transverse view in radiology convention (the top of the image represents the ventral side of human body, whereas the left-hand side denotes the right-hand side of the human body). (a) EIT temporary series images of tidal breath reconstructed based on three reconstruction methods. The impedance value of lung increases with air entering the lungs. Red and purple rectangular boxes represent peak expiratory and inspiratory images, respectively. (b) Intra-tidal difference images obtained by subtracting the peak expiratory image from the peak inspiratory image, i.e., the correlation value of regional lung ventilation volume; the area with 50% of maximum impedance is outlined in black. The color map at the bottom applies to all images. The temporal response of the TADI, LCV, and GCV methods required 18.12 ms, 1321.86 ms, and 1290.25 ms on average for each image reconstruction.

peak expiratory image from the peak inspiratory image in Fig. 11(b) indicated that the image reconstructed by the TADI algorithm was consistent with the shape of the lung, and the reconstructed signals were relatively concentrated and distributed on both the sides of the lung lobe. In contrast, the images reconstructed using the LCV and GCV methods produced varying degrees of deformation, including a larger number of reconstructed artifacts and divergent signals.

IV. DISCUSSION

In the development of EIT, several researchers have focused on increasing image reconstruction quality by selecting the optimal regularization parameters. However, the requirements for applications in clinical and experimental practice cannot be satisfied either by the heuristic experience method with strong subjectivity and poor consistency between various experiments and users, or the objective selection method with poor real-time monitoring efficiency and reliance on noise prior to information. Thus, this paper proposes the TADI algorithm based on dynamic linear approximation to increase the speed of image reconstruction and image quality. For the clinical application of EIT bedside monitoring, the proposed algorithm can realize real-time and continuous acquisition of high-quality reconstructed images by reducing the cost of complex manual operations such as the regularization parameter adjustment. Moreover, the reconstruction quality and generalization ability of the proposed algorithm was validated through comparisons with certain state-of-the-art methods under simulation, phantom experiment, and human lung recruitment data results.

A. ALGORITHM IMPLEMENTATION

In Section II, the mathematical derivation process demonstrated that the TADI algorithm proposed in this paper could reconstruct an improved target shape and smaller artifact interference. This was achieved as follows: (1) the use of a large regularization parameter correction regularization item to initiate the appropriate iteration smoothens the reconstruction target image and creates less number artifacts; (2) the algorithm converges globally with improved stability, and the iteration converges to the minimum point at all instances. Furthermore, the ill-condition in the image reconstruction process was effectively surpassed by retaining the contribution of the main low-order change information; (3) the algorithm was developed based on a robust principle to achieve an efficient calculation process, i.e., it is not necessary to select the optimal regularization parameters in advance from the complex objective regularization parameter selection method, including the manual revision of the iterative step size and direction in the calculation process.

B. PERFORMANCE OF TADI ALGORITHM

Based on literature review and prior experiments, we determined that the DLS algorithm is evidently advantageous in EIT image reconstruction (e.g., accurate positioning, fast imaging speed, and fewer artifacts), compared to the alternative methods. In the DLS algorithm, the Jacobian matrix was evaluated offline, and the reconstruction matrix was formed using the regularization parameters and matrix to ensure the real-time performance of the imaging. Nonetheless, a majority of the objective regularization parameter selection methods require the calculation of multiple conductivity change distribution images within a given range, and subsequently, the value of the most suitable imaging within the range is required to be determined as the optimal objective regularization parameter based on certain guidelines. The temporal response of the TADI algorithm totally satisfies the dynamic EIT clinical real-time requirements compared with the LCV and GCV methods.

In clinical EIT imaging monitoring, various conditions such as the measured boundary shape, electrode pattern, and additive noise may significantly influence the reconstruction quality. Therefore, in response to common conditions in the clinical EIT, we set up corresponding simulation, phantom experiment, and human lung recruitment data to verify the effectiveness and robustness of the algorithm in this study. Fig. 4–8 show that the proposed algorithm delivered superior imaging quality under various conditions. The reconstructed targets were more uniform and consistent, similar to the shape and size of the ground truth, and they exhibited improved distinguishability and recognition effects for multiple disturbance targets present in the region of interest. Furthermore, lesser number of artifacts were generated by the TADI algorithm in comparison to the two alternative methods.

C. LIMITATIONS OF STUDY

Although the proposed TADI algorithm offers significant advantages such as real-time performance and improved reconstruction quality, it was executed by setting the residual norm as the cost function and including the regularization term constraint to determine the minimum value, which applies a smoothing effect to the target boundary shape. In this study, the other weighted constraint term such as the L1 norm was not introduced in the algorithm. Compared with the L2 norm, the L1 norm reduced the deformation error and preserved the boundary. Therefore, the introduction of the additional norm to improve the reconstruction quality of the TADI algorithm requires further scientific research if the target is the lung, heart, or other anatomical structures depicting a more realistic distribution of electrical conductivity with sudden variations.

It should be noted that although the TADI algorithm has been used in simulation experiment to reconstruct EIT images under the 8-electrode, 16-electrode and 32-electrode configurations, more phantom and human data reconstruction experiments under different electrode distributions are still needed to verify the advantages of our algorithm. And a future research is to use the TADI algorithm for EIT image reconstruction under three-dimensional multilayer electrodes and open-electrodes configuration to prove the robustness and reliability of our algorithm.

Another limitation of this study is that it could not compare our reconstruction images with the ground truth of the chest to elaborate the EIT results in terms of size and shape. For EIT reconstruction of patients with different body shapes and different electrode distributions, it is effective to use the prior information provided by real images to improve the image quality. In the future, we will use our latest high-speed lung EIT system to compare real-time clinical EIT reconstruction images with CT and MRI images to improve the TADI algorithm.

V. CONCLUSION

In this study, we propose a novel algorithm for real-time bedside monitoring in practical imaging applications of clinical EIT. This algorithm uses dynamic linear approximation to improve imaging quality and reconstruction effectiveness without adjusting the regularization parameters, Furthermore, it can select the corresponding objective regularization parameters of the reconstructed images via norm fitting. The results of the simulation, phantom experiment, and human lung recruitment data established that the proposed algorithm yielded more stable results in the selection of regularization parameters than the conventional objective parameter selection method. Moreover, in terms of various complex conditions in the reconstruction of EIT targets, this algorithm achieved superior imaging quality under rapid reconstruction. In the future, this technology can be applied to more practical clinical problems, including embedding EIT imaging systems to explore more suitable regularization matrices for specific organs and tissues.

ACKNOWLEDGMENT

The authors would like to thank G. K. Wolf, C. Gómez-Laberge, J. N. Kheir, D. Zurakowski, B. K. Walsh, A. Adler, and J. H. Arnold for providing the open source EIT clinical data. All of the authors have no conflict of interests. *(Weirui Zhang and Tao Zhang contributed equally to this work.)*

REFERENCES

[1] A. Adler and A. Boyle, "Electrical impedance tomography: Tissue properties to image measures," *IEEE Trans. Biomed. Eng.*, vol. 64, no. 11, pp. 2494–2504, Nov. 2017.

[2] H. Li, R. Chen, C. Xu, B. Liu, X. Dong, and F. Fu, "Combing signal processing methods with algorithm priori information to produce synergetic improvements on continuous imaging of brain electrical impedance tomography," *Sci. Rep.*, vol. 8, no. 1, Jul. 2018, Art. no. 10086.

[3] M. Kircher, G. Elke, B. Stender, M. Hernandez Mesa, F. Schuderer, O. Dossel, M. K. Fuld, A. F. Halaweish, E. A. Hoffman, N. Weiler, and I. Frerichs, "Regional lung perfusion analysis in experimental ARDS by electrical impedance and computed tomography," *IEEE Trans. Med. Imag.*, vol. 40, no. 1, pp. 251–261, Jan. 2021.

[4] L. Yang, M. Dai, S. Li, H. Wang, X. Cao, and Z. Zhao, "Real-time assessment of global and regional lung ventilation in the anti-gravity straining maneuver using electrical impedance tomography," *Comput. Biol. Med.*, vol. 135, Aug. 2021, Art. no. 104592.

[5] I. Frerichs, M. B. Amato, A. H. van Kaam, D. G. Tingay, Z. Zhao, B. Grychtol, M. Bodenstein, H. Gagnon, S. H. Bohm, E. Teschner, O. Stenqvist, T. Mauri, V. Torsani, L. Camporota, A. Schibler, G. K. Wolf, D. Gommers, S. Leonhardt, and A. Adler, "Chest electrical impedance tomography examination, data analysis, terminology, clinical use and recommendations: Consensus statement of the translational EIT development study group," *Thorax*, vol. 72, no. 1, pp. 83–93, 2017.

[6] E. K. Murphy, A. Mahara, and R. J. Halter, "Absolute reconstructions using rotational electrical impedance tomography for breast cancer imaging," *IEEE Trans. Med. Imag.*, vol. 36, no. 4, pp. 892–903, Apr. 2017.

[7] F. You, X. Shi, W. Shuai, H. Zhang, W. Zhang, F. Fu, R. Liu, C. Xu, T. Bao, and X. Dong, "Applying electrical impedance tomography to dynamically monitor retroperitoneal bleeding in a renal trauma patient," *Intensive Care Med*, vol. 39, no. 6, pp. 1159–1160, Jun. 2013.

[8] D. Meroni, C. C. Maglioli, D. Bovio, F. G. Greco, and A. Aliverti, "An electrical impedance tomography (EIT) multi-electrode needle-probe device for local assessment of heterogeneous tissue impeditivity," in *Proc. 39th Annu. Int. Conf. IEEE Eng. Med. Biol. Soc. (EMBC)*, Jul. 2017, pp. 1385–1388.

[9] H. Li, R. Chen, C. Xu, B. Liu, M. Tang, L. Yang, X. Dong, and F. Fu, "Unveiling the development of intracranial injury using dynamic brain EIT: An evaluation of current reconstruction algorithms," *Physiol. Meas.*, vol. 38, no. 9, pp. 1776–1790, Sep. 2017.

[10] B. Yang, B. Li, C. Xu, S. Hu, M. Dai, J. Xia, P. Luo, X. Shi, Z. Zhao, X. Dong, Z. Fei, and F. Fu, "Comparison of electrical impedance tomography and intracranial pressure during dehydration treatment of cerebral edema," *NeuroImage, Clin.*, vol. 23, Jan. 2019, Art. no. 101909.

[11] Y. Li, D. Zhang, B. Liu, Z. Jin, W. Duan, X. Dong, F. Fu, S. Yu, and X. Shi, "Noninvasive cerebral imaging and monitoring using electrical impedance tomography during total aortic arch replacement," *J. Cardiothoracic Vascular Anesthesia*, vol. 32, no. 6, pp. 2469–2476, Dec. 2018.

[12] G. Liang, S. Ren, and F. Dong, "A shape-based statistical inversion method for EIT/URT dual-modality imaging," *IEEE Trans. Image Process.*, vol. 29, pp. 4099–4113, 2020.

[13] E. K. Murphy, A. Mahara, and R. J. Halter, "A novel regularization technique for microendoscopic electrical impedance tomography," *IEEE Trans. Med. Imag.*, vol. 35, no. 7, pp. 1593–1603, Jul. 2016.

[14] M. Fernández-Corazza, S. Turovets, P. Luu, N. Price, C. Horacio Muravchik, and D. Tucker, "Skull modeling effects in conductivity estimates using parametric electrical impedance tomography," *IEEE Trans. Biomed. Eng.*, vol. 65, no. 8, pp. 1785–1797, Aug. 2018.

[15] F. Braun, M. Proença, M. Lemay, M. Bertschi, A. Adler, J.-P. Thiran, and J. Solà, "Limitations and challenges of EIT-based monitoring of stroke volume and pulmonary artery pressure," *Physiolog. Meas.*, vol. 39, no. 1, Jan. 2018, Art. no. 014003.

[16] B. Hentze, T. Muders, C. Hoog Antink, C. Putensen, A. Larsson, G. Hedenstierna, M. Walter, and S. Leonhardt, "A model-based source separation algorithm for lung perfusion imaging using electrical impedance tomography," *Physiolog. Meas.*, vol. 42, no. 8, Aug. 2021, Art. no. 084001.

[17] B. McDermott, A. Elahi, A. Santorelli, M. O'Halloran, J. Avery, and E. Porter, "Multi-frequency symmetry difference electrical impedance tomography with machine learning for human stroke diagnosis," *Physiolog. Meas.*, vol. 41, no. 7, Aug. 2020, Art. no. 075010.

[18] D. Calvetti, S. Nakkireddy, and E. Somersalo, "A Bayesian filtering approach to layer stripping for electrical impedance tomography," *Inverse Problems*, vol. 36, no. 5, May 2020, Art. no. 055014.

[19] Y. W. Wen and R. H. Chan, "Parameter selection for total-variation-based image restoration using discrepancy principle," *IEEE Trans. Image Process.*, vol. 21, no. 4, pp. 1770–1781, Apr. 2012.

[20] F. Braun, M. Proenca, J. Sola, J.-P. Thiran, and A. Adler, "A versatile noise performance metric for electrical impedance tomography algorithms," *IEEE Trans. Biomed. Eng.*, vol. 64, no. 10, pp. 2321–2330, Oct. 2017.

[21] R. P. K. Jagannath and P. K. Yalavarthy, "Minimal residual method provides optimal regularization parameter for diffuse optical tomography," *J. Biomed. Opt.*, vol. 17, no. 10, Oct. 2012, Art. no. 106015.

[22] N. Sella, T. Pettenuzzo, F. Zarantonello, G. Andreatta, A. De Cassai, C. Schiavolin, C. Simoni, L. Pasin, A. Boscolo, and P. Navalesi, "Electrical impedance tomography: A compass for the safe route to optimal PEEP," *Respiratory Med.*, vol. 187, Jul. 2021, Art. no. 106555.

[23] G. Y. Jang, G. Ayoub, Y. E. Kim, T. I. Oh, C. R. Chung, G. Y. Suh, and E. J. Woo, "Integrated EIT system for functional lung ventilation imaging," *Biomed. Eng. OnLine*, vol. 18, no. 1, pp. 1–18, Dec. 2019.

[24] T. Zhang, X. Liu, W. Zhang, M. Dai, C. Chen, X. Dong, R. Liu, and C. Xu, "Adaptive threshold split Bregman algorithm based on magnetic induction tomography for brain injury monitoring imaging," *Physiolog. Meas.*, vol. 42, no. 6, May 2021, Art. no. 065004.

[25] Y. Mamatjan, A. Borsic, D. Gursoy, and A. Adler, "An experimental clinical evaluation of EIT imaging with ℓ_1 data and image norms," *Physiolog. Meas.*, vol. 34, no. 9, pp. 1027–1039, Sep. 2013.

[26] X. Liu, H. Li, H. Ma, C. Xu, B. Yang, M. Dai, X. Dong, and F. Fu, "An iterative damped least-squares algorithm for simultaneously monitoring the development of hemorrhagic and secondary ischemic lesions in brain injuries," *Med. Biol. Eng. Comput.*, vol. 57, no. 9, pp. 1917–1931, Sep. 2019.

[27] D. M. Nguyen, P. Qian, T. Barry, and A. McEwan, "Self-weighted NOSER-prior electrical impedance tomography using internal electrodes in cardiac radiofrequency ablation," *Physiolog. Meas.*, vol. 40, no. 6, Jul. 2019, Art. no. 065006.

[28] E. K. Murphy, A. Mahara, X. Wu, and R. J. Halter, "Phantom experiments using soft-prior regularization EIT for breast cancer imaging," *Physiol. Meas.*, vol. 38, pp. 1262–1277, May 2017.

[29] S. Liu, J. Jia, Y. D. Zhang, and Y. Yang, "Image reconstruction in electrical impedance tomography based on structure-aware sparse Bayesian learning," *IEEE Trans. Med. Imag.*, vol. 37, no. 9, pp. 2090–2102, Sep. 2018.

[30] T. Correia, A. Gibson, M. Schweiger, and J. Hebden, "Selection of regularization parameter for optical topography," *J. Biomed. Opt.*, vol. 14, no. 3, 2009, Art. no. 034044.

[31] J. F. Abascal, S. R. Arridge, R. H. Bayford, and D. S. Holder, "Comparison of methods for optimal choice of the regularization parameter for linear electrical impedance tomography of brain function," *Physiol. Meas.*, vol. 29, no. 11, pp. 1319–1334, Nov. 2008.

[32] B. Gong, B. Schullcke, S. Krueger-Ziolek, F. Zhang, U. Mueller-Lisse, and K. Moeller, "Higher order total variation regularization for EIT reconstruction," *Med. Biol. Eng. Comput.*, vol. 56, no. 8, pp. 1367–1378, Jan. 2018.

[33] M. Chen, H. Su, Y. Zhou, C. Cai, D. Zhang, and J. Luo, "Automatic selection of regularization parameters for dynamic fluorescence molecular tomography: A comparison of L-curve and U-curve methods," *Biomed. Opt. Exp.*, vol. 7, no. 12, pp. 5021–5041, Dec. 2016.

[34] A. Adler, J. H. Arnold, R. Bayford, A. Borsic, B. Brown, P. Dixon, T. J. C. Faes, I. Frerichs, H. Gagnon, Y. Gärber, B. Grychtol, G. Hahn, W. R. B. Lionheart, A. Malik, R. P. Patterson, J. Stocks, A. Tizzard, N. Weiler, and G. K. Wolf, "GREIT: A unified approach to 2D linear EIT reconstruction of lung images," *Physiolog. Meas.*, vol. 30, no. 6, pp. S35–S55, Jun. 2009.

[35] A. Witkowska-Wrobel, K. Aristovich, A. Crawford, J. D. Perkins, and D. Holder, "Imaging of focal seizures with electrical impedance tomography and depth electrodes in real time," *NeuroImage*, vol. 234, Jul. 2021, Art. no. 117972.

[36] S. Xuetao, Y. Fusheng, F. Feng, L. Ruigang, and D. Xiuzhen, "High precision multifrequency electrical impedance tomography system and preliminary imaging results on saline tank," in *Proc. IEEE Eng. Med. Biol. 27th Annu. Conf.*, Jan. 2005, pp. 1492–1495.

[37] L. Gattinoni, A. Protti, P. Caironi, and E. Carlesso, "Ventilator-induced lung injury: The anatomical and physiological framework," *Crit. Care Med.*, vol. 38, pp. S539–S548, Oct. 2010.

[38] L. Yang, M. Dai, K. Möller, I. Frerichs, A. Adler, F. Fu, and Z. Zhao, "Lung regions identified with CT improve the value of global inhomogeneity index measured with electrical impedance tomography," *Quant. Imag. Med. Surg.*, vol. 11, no. 4, pp. 1209–1219, Apr. 2021.

[39] C. Gomez-Laberge, J. H. Arnold, and G. K. Wolf, "A unified approach for EIT imaging of regional overdistension and atelectasis in acute lung injury," *IEEE Trans. Med. Imag.*, vol. 31, no. 3, pp. 834–842, Mar. 2012.

[40] G. K. Wolf, C. Gomez-Laberge, J. N. Kheir, D. Zurakowski, B. K. Walsh, A. Adler, and J. H. Arnold, "Reversal of dependent lung collapse predicts response to lung recruitment in children with early acute lung injury," *Pediatric Crit. Care Med.*, vol. 13, no. 5, pp. 509–515, Sep. 2012.

WEIRUI ZHANG was born in Tongling, Anhui, China, in 1996. He received the B.S. degree in biomedical engineering from Fourth Military Medical University, Xi'an, China, in 2018, where he is currently pursuing the M.S. degree in biomedical engineering.

From 2018 to 2019, he was a Research Assistant with the Institute of Biomedical Engineering, Fourth Military Medical University. He is the author of ten articles and two inventions. His research interests include the development of biological/medical imaging techniques using electrical impedance tomography (EIT) and fundamental study of biomedical signal processing and analysis.

TAO ZHANG received the B.S. degree in biomedical engineering from Fourth Military Medical University, Xi'an, China, in 2016, where he is currently pursuing the M.S. degree, under the supervision of Prof. Canhua Xu. Since 2016, he has been working as an Assistant Engineer at the Drug and Instrument Supervision and Inspection Station. His research interest includes magnetic induction tomography reconstruction algorithm.

XUECHAO LIU received the B.S. degree in communication engineering from the Ocean University of China, Qingdao, China, in 2016, and the M.S. degree from the School of Biomedical Engineering, Fourth Military Medical University, in 2019. She is currently an Assistant with the Department of Biomedical Engineering, Fourth Military Medical University. Her research interest includes electromagnetic tomography reconstruction algorithm.

BIN YANG was born in Xi'an, China, in 1978. He received the M.Sc. degree in cell biology and the Ph.D. degree in biomedical engineering from Fourth Military Medical University, Xi'an, in 2007 and 2013, respectively. Since 2019, he has been an Assistant Professor with the Department of Biomedical Engineering, Air Force Military Medical University. He has a strong interest in exploration of interdisciplinary fields between engineering and medicine. His research interests include electrical impedance tomography and biomedical signal processing and design of advanced medical devices.

MENG DAI was born in Shaanxi, China, in 1982. He received the B.S., M.S., and M.D. degrees in biomedical engineering from Fourth Military Medical University, Xi'an, China, in 2006, 2009, and 2012, respectively. He is currently an Associate Professor with the Department of Biomedical Engineering, Fourth Military Medical University. His current research interests include electrical impedance measurement and imaging.

XUETAO SHI was born in China, in 1973. He received the B.S., M.S., and Ph.D. degrees in biomedical engineering from Fourth Military Medical University, Xi'an, China, in 1995, 2001, and 2006, respectively. He is currently a Professor with the Department of Biomedical Engineering, Fourth Military Medical University. His current research interests include the measurement and analysis of dielectric properties of tissues, bioimpedance measurement, and imaging monitoring by electrical impedance tomography.

XIUZHEN DONG (Member, IEEE) was born in China, in 1945. She received the B.S. degree in automatic control from Harbin Military Engineering University, Harbin, China, in 1968. Since 1994, she has been a Professor at Fourth Military Medical University, Xi'an, China, where she has also been a Doctoral Advisor, since 1998. She is the author or the coauthor of more than 200 papers published in international journals and conferences. Her current research interests include electrical impedance tomography and biomedical signal detection and processing.

FENG FU received the B.S., M.S., and M.D. degrees in biomedical engineering from Fourth Military Medical University, Xi'an, China, in 1993, 1996, and 1999, respectively. He is currently a Professor with the Department of Biomedical Engineering, Fourth Military Medical University. His current research interests include electrical impedance measurement and imaging.

CANHUA XU was born in Leping, Jiangxi, China, in 1984. He received the B.S. degree in biomedical engineering, in 2004, and the Ph.D. degree in biomedical engineering from Fourth Military Medical University, Xi'an, China, in 2010.

From 2010 to 2015, he was a Lecturer with Fourth Military Medical University. Since 2015, he has been an Assistant Professor with the Biomedical Engineering School, Fourth Military Medical University. His research interests include image reconstruction algorithm, electrical impedance tomography, and magnetic induction tomography.